Coordination environment-tailored electronic structure of single atomic copper sites for efficient electrochemical nitrate reduction toward ammonia

Tianchi Huang, Taiyu Liang, Jiao You, Qihua Huo, Shuai Qi, Jingwen Zhao, Na Meng, Jinglian Liao, Chunyan Shang, Hengpan Yang, Qi Hu* and Chuanxin He*

Experimental Section

Materials

Copper nitrate trihydrate (Cu $(NO_3)_2 \cdot 3H_2O$), Boric acid (H_3BO_3) and melamine ($C_3H_6N_6$) were purchased from Aladdin Chemical Reagent Co., Ltd (Shanghai, China). Porous carbon was purchased from Nanjing XFNANO Materials Tech Co., Ltd (Nanjing, China). All chemicals were analytical grade and used as received without further purification. Deionized water was used in all experiments.

Synthesis of catalysts

Cu-N$_4$B$_2$ catalyst. Typically, 20 mg of Cu $(NO_3)_2 \cdot 3H_2O$, 90 mg of melamine, 180 mg of boric acid and 180 g microporous carbon were well dispersed in 5 ml deionized water under sonicated bath for 1 h to obtain a homogenous black suspension, which was then centrifuged and washed for 3 times, and the obtained precipitate was dried at 60 °C for 24 h. The powder was collected and heated in N_2 at 800 ºC for 1 h with a heating rate of 5 ºC /min. After that the collected sample was denoted as Cu-N$_4$B$_2$. For N/B ratio of 1:1 and N/B ratio of 1:3 samples, the added amount of boric acid was changed to 90 and 270 mg, respectively, and the preparation route was the same as that of Cu-N$_4$B$_2$.

Cu-N$_4$ catalyst. The synthesis procedure of the Cu-N$_4$ catalyst was similar to that of

Cu-N$_4$B$_2$ but without the addition of boric acid.

Materials Characterizations

Physical characterizations.

The X-ray diffraction (XRD) patterns were analyzed using a D8ADVANCE diffractometer with Kα radiation. The morphology and microstructure of the samples were characterized by transmission electron microscopy and HAADF-STEM (JEOL JEM-ARF200, Titan Cubed Themis G2300). XPS analysis was conducted using a Thermo VG ESCALAB250 X-ray photoelectron spectrometer to determine the chemical valences of various elements. The specific surface area of the samples was measured using a Micromeritics ASAP 2460 instrument. The UV-vis spectrophotometer (UV-2550; Shimadzu, Kyoto, Japan) was used for product concentration measurements. X-ray absorption spectroscopy (XAS) tests were performed on a Spring 8 14b2, where a pair of channel-cut Si (111) crystals were used for the monochromator. The operating parameters were the operating energy of the storage ring of 8.0 GeV and the average electron current of 99.5 mA, respectively. Thus, X-ray adsorption near edge structure (XANES) and extended X-ray fine structure (EXAFS) data information can be obtained.

In-situ ATR-SEIRAS.

Attenuated total reflection surface enhanced Infrared absorption spectroscopy (ATR-SEIRAS) experiments were performed on a BRUKER INVENIO-S FT-IR spectrometer equipped with a liquid nitrogen cooled MCT detector and a PIKE VeeMAX III variable Angle ATR sampling attachment. Spectra were acquired at 0 V to -0.8 V with RHE. Each spectrum was acquired using a liquid argon cold mid-band cadmium mercury-telluride (MCT) detector with a resolution of 4 cm^{-1} and an average of 128 scans.

Differential electrochemical mass spectrometry (DEMS) measurements.

DEMS measurements were performed using Linglu Instruments QAS100, where the

Ar was continuously bubbled into 1 M KOH electrolyte and 0.1 M KNO_3 electrolyte before and during the measurements. Pt wire and saturated calomel electrode (SCE) were used as working electrode, counter electrode and reference electrode, respectively, on gold coated $Cu-N_4$ and $Cu-N_4B_2$ electrocatalyst. The linear scan voltammetry technique was applied at a scan rate of 10 mV s-1 at a scan rate of 0 to -0.8 V with RHE until the baseline remained stable. Then, the corresponding quality signal appears. After the electrochemical test, the mass signal returns to baseline and the next cycle starts. After six cycles, the experiment ended.

Electrochemical Measurements.

The three-electrode system in the H-type cell was used for NO_3^-RR measurements via an electrochemical station (CHI 760 E, CH Instrument Inc). In this typical three-electrode system, carbon paper was used as the working electrode (0.5×0.5 cm) and the electrocatalyst ink was drip-coated on the carbon paper (2 mg cm^{-2}). To prepare the electrocatalyst ink, 2 mg of the catalyst was dispersed into a 200 ul mixed solution containing ethanol, water, and Nafion at a ratio of 45:4:1, followed by a 40-min ultrasonic dispersion treatment to obtain a homogeneous solution. The reference electrode was Hg/HgO (saturated with 1M KOH), the counter electrode was platinum foil, and the electrolyte was 1M KOH and 0.1M KNO_3 mixed aqueous solution. The corresponding LSV curves were measured at a scan rate of 5 mV s^{-1}, and the Cdl in the potential range with almost zero Faraday current density was obtained by cyclic voltammetry (CV). All measured potentials were converted to reversible hydrogen electrodes (RHE) according to the Nernst equation: $E_{RHE} = E_{Hg/HgO}+0.098+0.0591pH$ (pH =14). If not specified, all linear voltammetric sweep curves (LSV) are corrected for iR_s compensation, where R_s is the solution resistance (Ω) between the working and reference electrodes. Argon gas was pumped uninterrupted into the cathode side of the H-cell to eliminate the effect of air. Electrical impedance spectroscopy (EIS) tests were performed in the range of 0.1 Hz to 10^5 Hz.

NH_3 efficiency calculations.

The Faraday efficiency of ammonia (FE_{NH3}) is calculated according to the following formula:

$$FE_{NH3} = \frac{nV_{catholyte}C_{NH3}F}{Q}$$

The n is the transferred electron number for the generation of 1 mol ammonia, here is 8; $V_{catholyte}$ is the liquid product volume (L), the value is 0.04 L; C_{NH3} is the detected ammonia (M) concentration in liquid products; F is the Faraday constant (96485 C·mol⁻¹); Q indicates the total charge consumed (Q = it).

NH₃ detection.

The indole phenol blue method was used to accurately quantify the NH_3 produced in the electrolyte. The electrolyte, which was continuously electrolytic for 1 h, was diluted in equal proportions with 1 M KOH to ensure that the ammonia gas concentration in the obtained electrolyte product fell within the linear range of the indoxyl blue method. Subsequently, 0.036 mol salicylic acid, 0.018 mol potassium sodium tartrate tetrahydrate, and 0.036 mol sodium hydroxide were mixed with 100 ml deionized water to prepare the colorant. Then, 4 mL of diluted liquid product, 500 μL of colorant, 50 μL NaClO (6-14% available chlorine), and 50 μL NaOH solution (0.75 M) were mixed together and allowed to stand in the dark for 30 minutes. Finally, the absorption spectrum was determined using a UV-vis spectrophotometer. The concentration of NH_3 was measured by the absorbance at ~655nm.

¹H NMR spectroscopy.

To assess NH_3 production, isotope-labeled tracer experiments were conducted using a 100 mM $^{15}NO_3^-$ solution as the nitrogen source. The quantification of NH3 generated involved further analysis through proton nuclear magnetic resonance (¹H NMR) spectroscopy. The specific procedure entailed the selection of malic acid as an internal standard. Next, a mixture of 100 μL malic acid (3.2 mM), 300 μL NO_3^-RR post-electrolyte, 100 μL H_2SO_4 aqueous solution (4 M), and 100 μL D_2O was thoroughly blended. After the addition of tetramethylsilane, the mixture was transferred to an NMR tube, sealed, and measured using an NMR spectrometer to obtain 1H NMR spectra. The

concentration of NH_3 was determined by analyzing the integration region of malic acid and ammonium vinyl singlet ammonium.

NO_2^- detection.

Griess method was used to detect NO_2^- in liquid products. Firstly, N- (1-naphthyl) ethylenediamine dihydrochloride (0.1 g) and sulfamethoxazole (1 g) were dissolved in deionized water (50 mL), and then H_3PO_4 (2.94 mL) was slowly added into the above solution, and the detection solution was obtained after full dissolution. Then, 2 mL of the colorant and 2 mL of the liquid product were mixed together and left in the dark for 15 min to obtain a fully stained solution. Finally, the concentration of NO_2^- was determined by the peak at ~540 nm in the absorption spectrum measured by the UV-vis spectrophotometer

Computational Details.

First-principle calculations were performed by the density functional theory (DFT) using the Vienna Ab-initio Simulation Package (VASP) package [1]. The generalized gradient approximation (GGA) with the Perdew-Burke-Ernzerhof (PBE) functional were used to describe the electronic exchange and correlation effects [2]. Uniform G-centered k-points meshes with a resolution of $2\pi*0.04$ Å^{-1} with Methfessel-Paxton electronic smearing were adopted in the Brillouin zone for geometric optimization. The simulation was run with a cutoff energy of 500 eV throughout the computations. The total energy and force thresholds for geometry optimizations were $1*10^{-5}$ eV and 0.05 eV Å^{-1}, respectively. A vacuum distance of 15 Å was set to ensure sufficient vacuum and avoid interactions between two periods. The DFT-D2 Van der Walls correction by Grimme [3] was also considered in all calculations. The H_2O dissociation energy was estimated using the Nudged Elastic Band (NEB) method.[4]
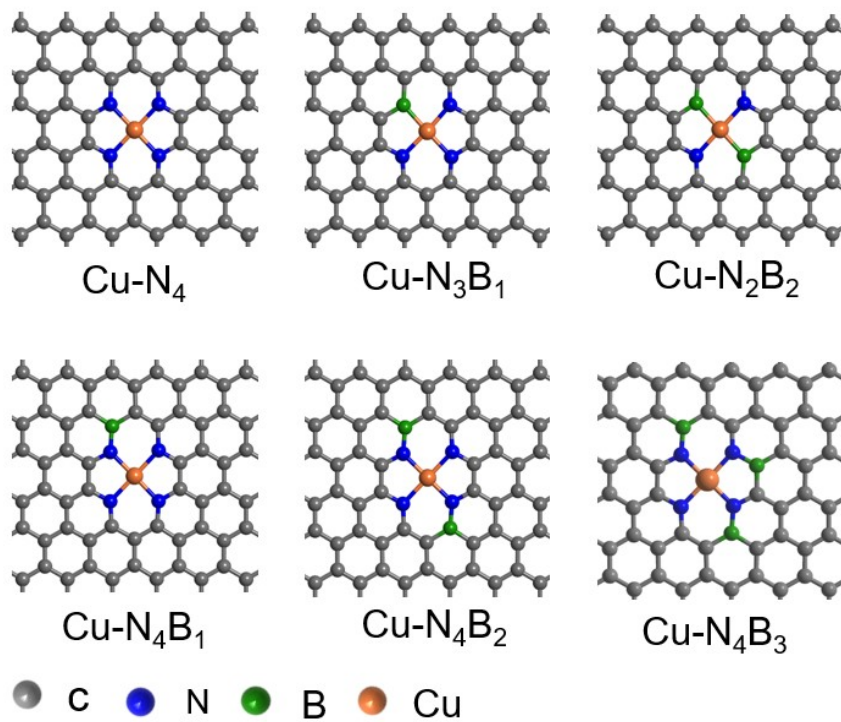
Figure S1 $Cu-N_4$, $Cu-N_3B$, $Cu-N_2B_2$, $Cu-N_4B_1$, $Cu-N_4B_2$ and $Cu-N_4B_3$ models.
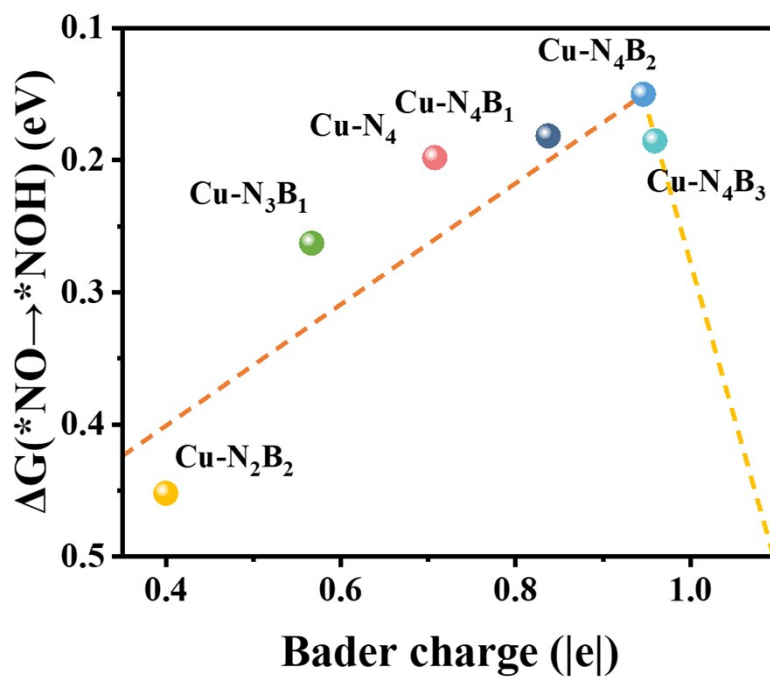
Figure S2 Correlation of Cu bader charge and $\Delta G(*NO \rightarrow *NOH)$ on Cu-N$_4$, Cu-N$_4$B$_2$, Cu-N$_2$B$_2$, Cu-N$_3$B$_1$, Cu-N$_4$B$_2$ and Cu-N$_4$B$_3$ models.
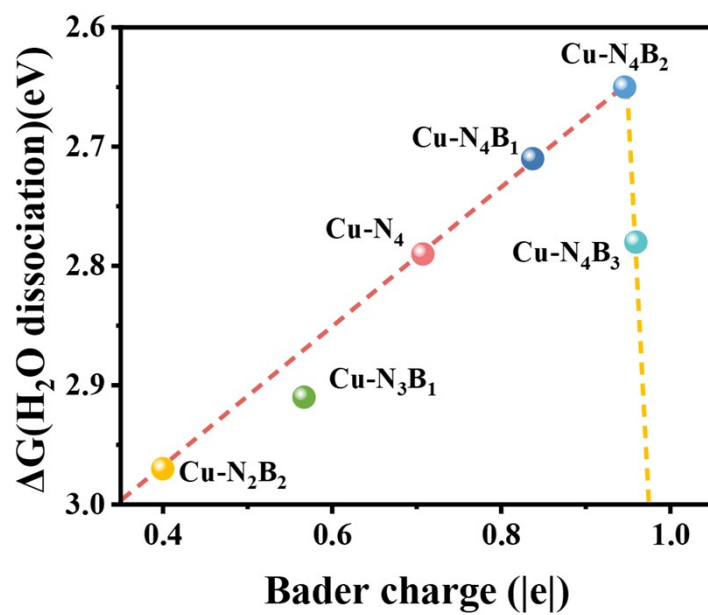
Figure S3 Correlation of Cu bader charge and energy barrier of water dissociation on Cu-N$_4$, Cu-N$_4$B$_2$, Cu-N$_2$B$_2$, Cu-N$_3$B$_1$, Cu-N$_4$B$_2$ and Cu-N$_4$B$_3$ models.**.**
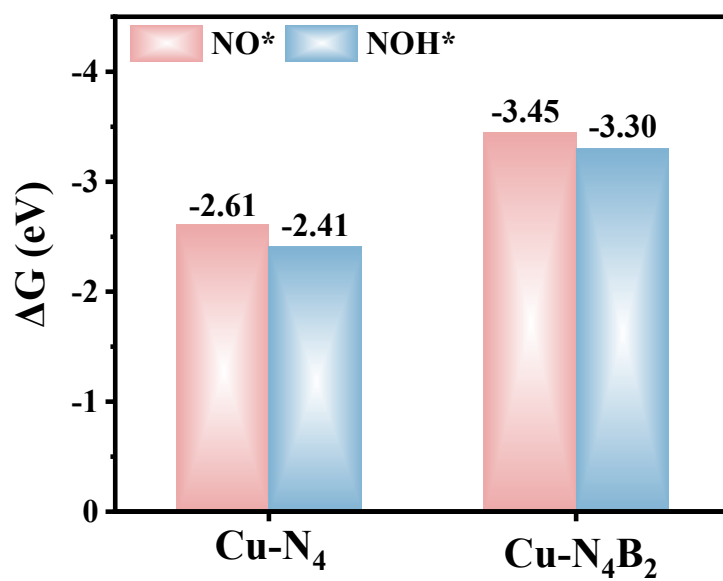
Figure S4 Free adsorption energy of *NO and *NOH on Cu-N_4 and Cu-N_4B_2.
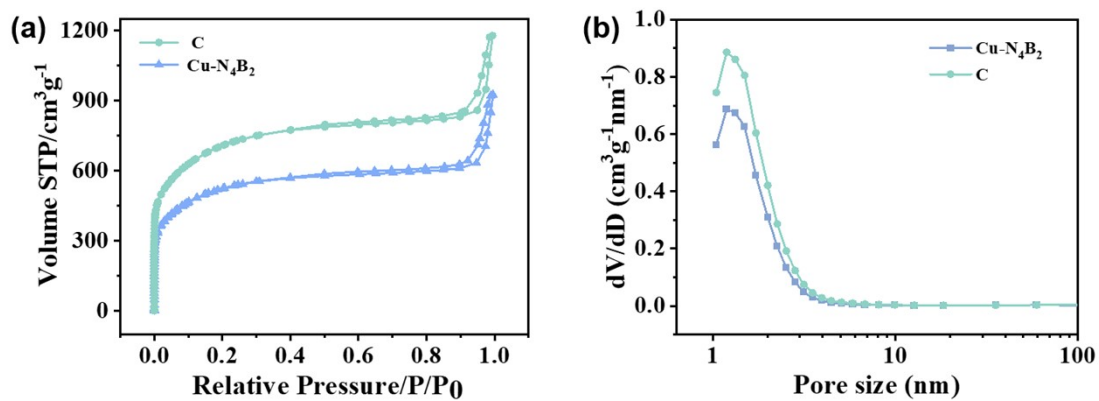
Figure S5 N_2 adsorption/desorption isotherms (a) and pore distribution curves (b) of the Cu-N_4B_2 and C.
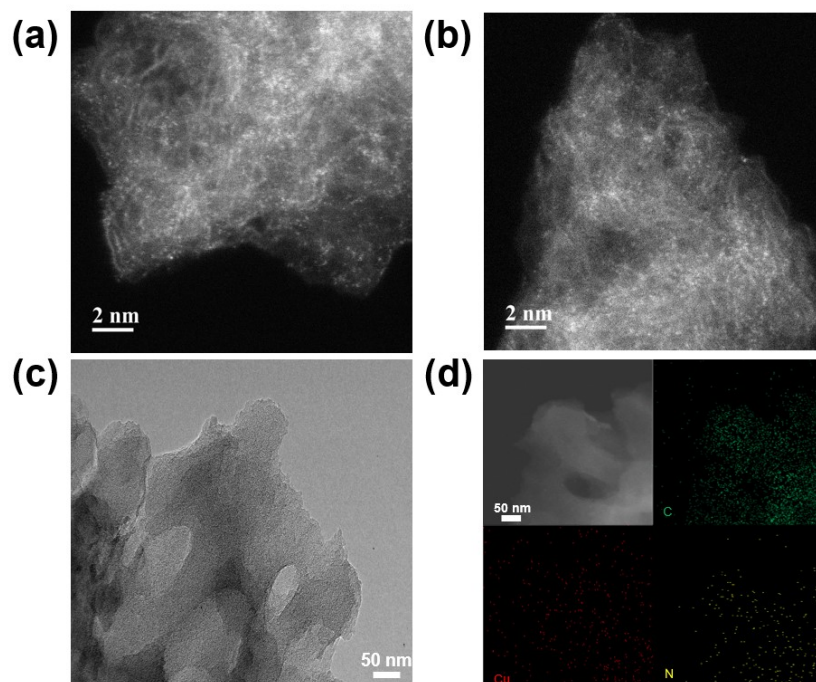
Figure S6 (a-b) AC-HAADF-STEM of Cu-N$_4$ (c) TEM of Cu-N$_4$ (d) EDS element mapping images of Cu-N$_4$.
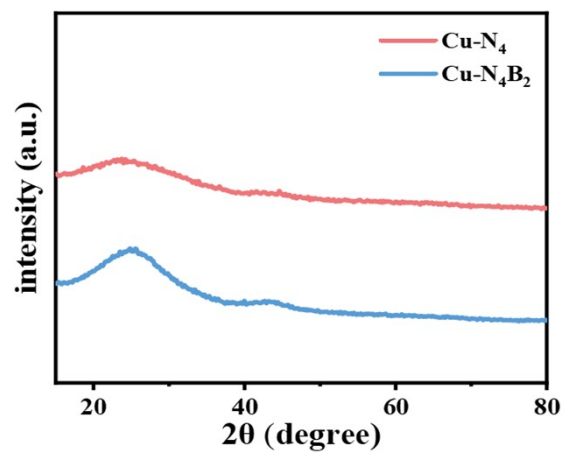
Figure S7 XRD patterns of Cu-N$_4$ and Cu-N$_4$B$_2$.
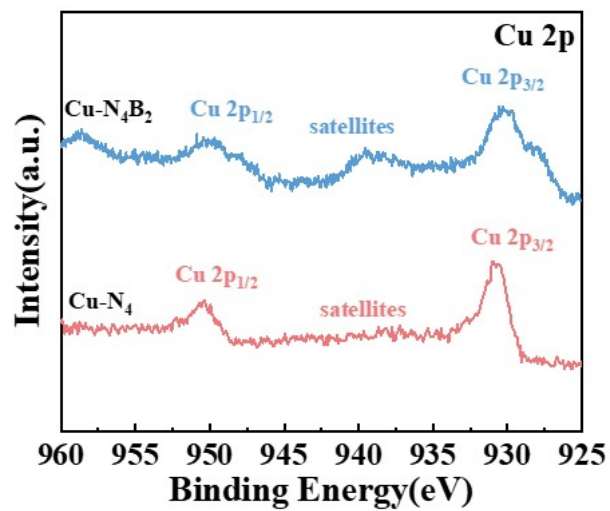
Figure S8 XPS spectra of Cu 2p for Cu-N$_4$B$_2$ and Cu-N$_4$.
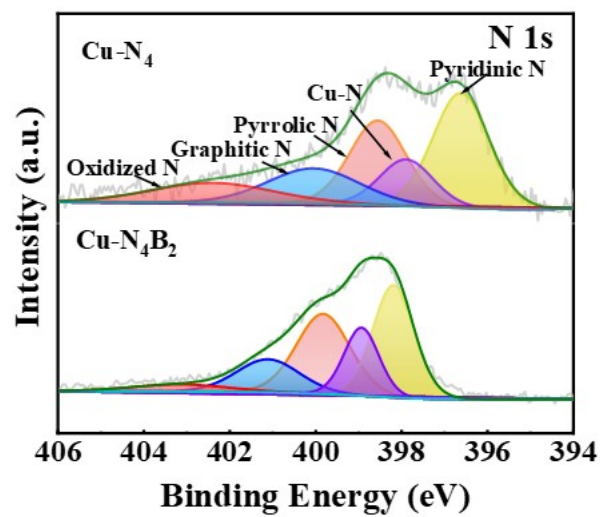
Figure S9 XPS spectra of N 1s for Cu-N$_4$B$_2$ and Cu-N$_4$.
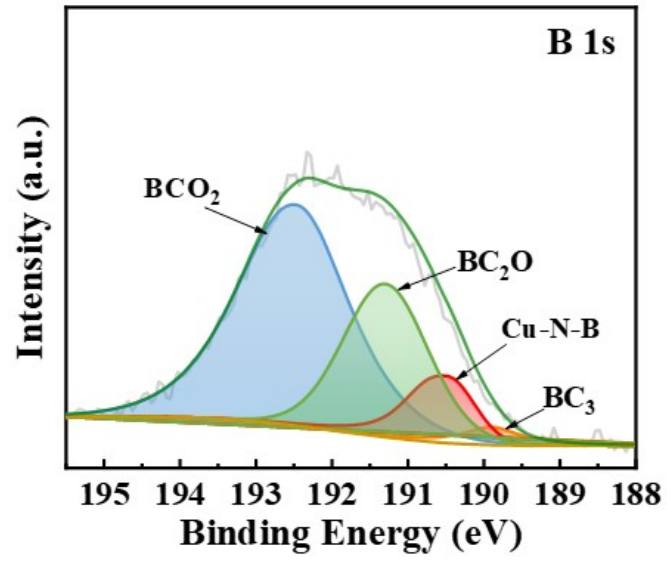
Figure S10 XPS spectrum of B 1s for Cu-N$_4$B$_2$.
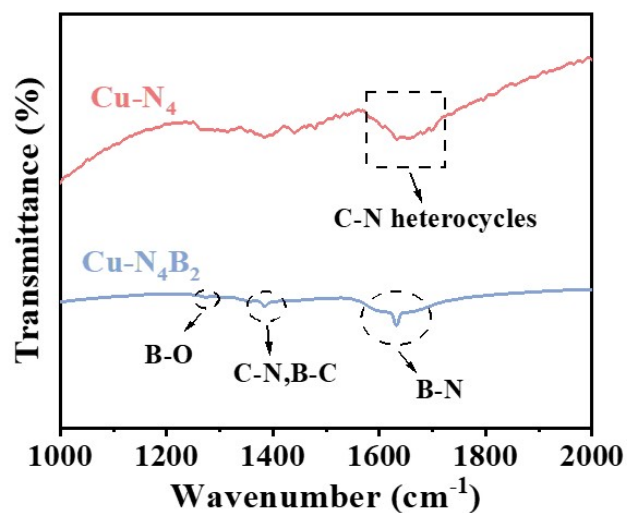
Figure S11 FTIR spectra of Cu-N$_4$B$_2$ and Cu-N$_4$. FTIR spectrum of Cu-N$_4$B$_2$ showed the characteristic peaks of B-N bonds around 1650 cm^{-1}. Peaks corresponding to C-N and C-B could also be seen from 1390 to 1430 cm^{-1}. A small peak at 1280 cm^{-1} was ascribed to B-O bonds. While FTIR spectrum of N-Cu only showed typical peaks of C-N heterocycles
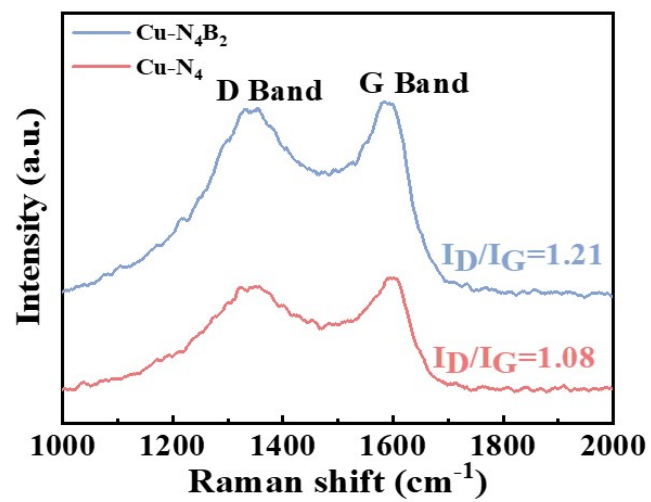
Figure S12 Raman spectra of the Cu-N$_4$B$_2$ and Cu-N$_4$.
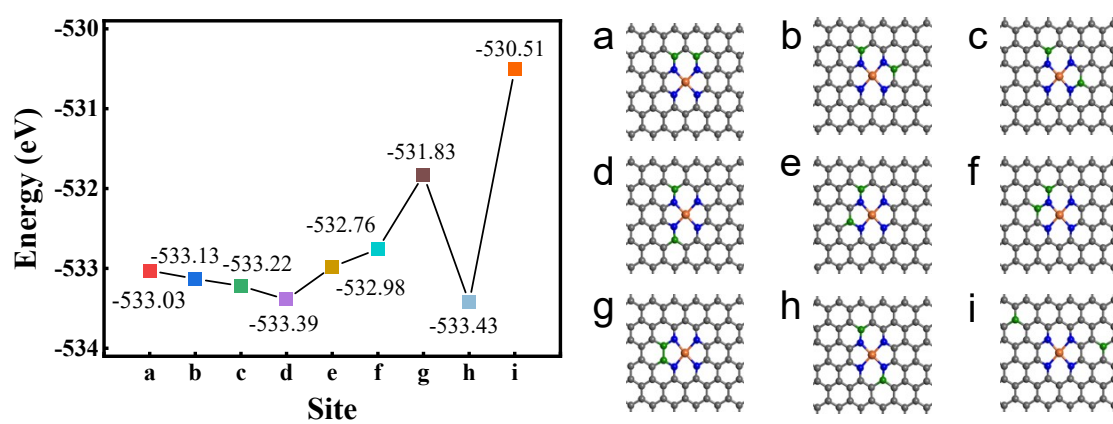
Figure S13 The energy of different CuN_4B_2 configurations and related structure diagrams.
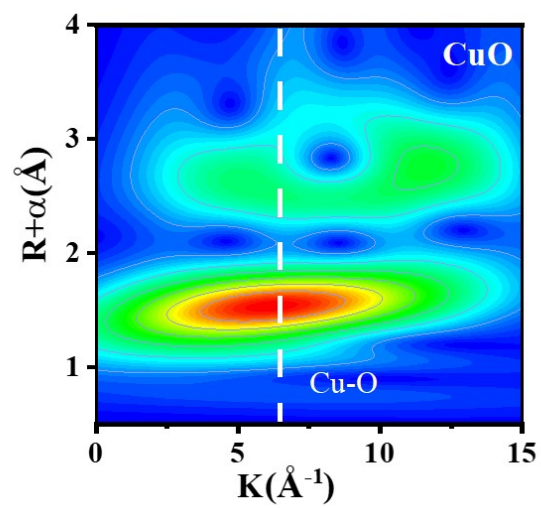
Figure S14 The WT-EXAFS images of CuO.
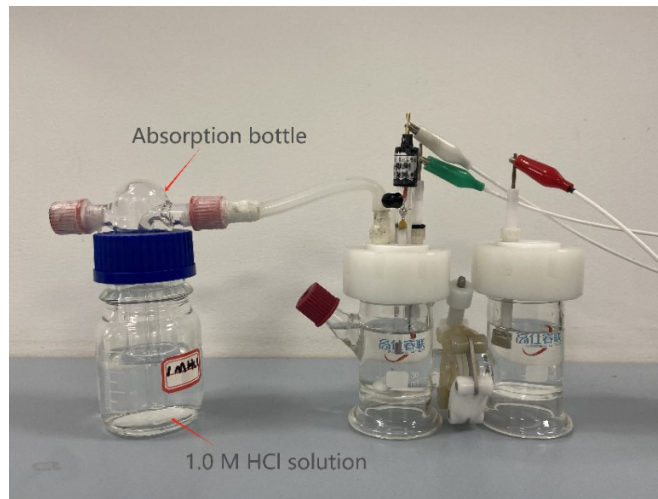
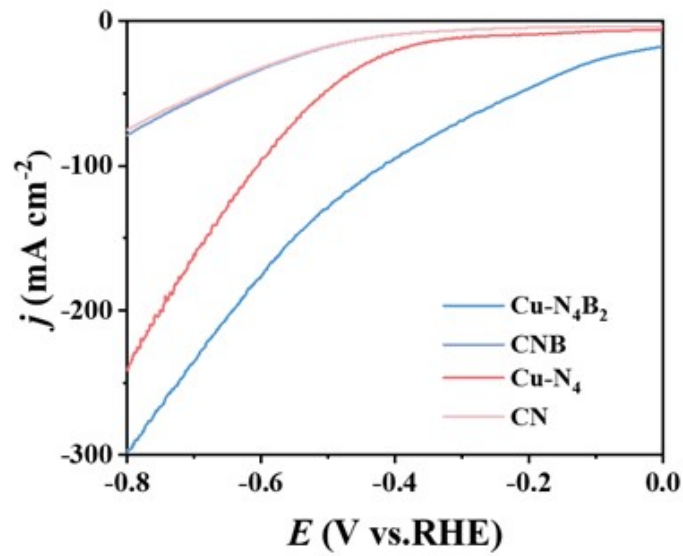**Figure 15** Schematic diagram of NH$_3$ gas capture device.

Figure S16 LSV curves of Cu-N$_4$B$_2$, CN$_4$B$_2$, Cu-N$_4$ and CN in NO$_3^-$-saturated electrolyte. CN is nitrogen doped on graphite carbon, and BCN is boron nitrogen codoped on graphite carbon.
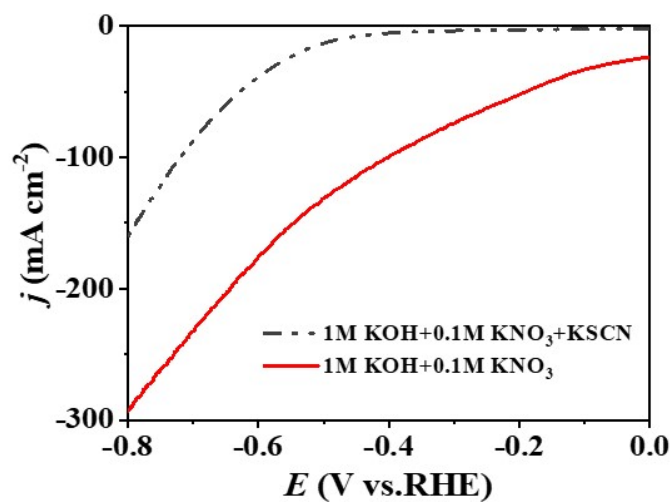
Figure 17 Polarization curves of Cu-N$_4$B$_2$ recorded with and without introduction of cyanate ions (SCN$^-$) into Ar-saturated 1 M KOH and 0.1 M KNO$_3$ at a sweep rate of 1 mV s^{-1}. The NO$_3^-$RR current of Cu-N$_4$B$_2$ decreases drastically with the addition of SCN$^-$ ions, which are known as a metal center poisoner, confirming that Cu single atoms serve as the active sites for NO$_3^-$RR. All the data were collected with i-R correction.
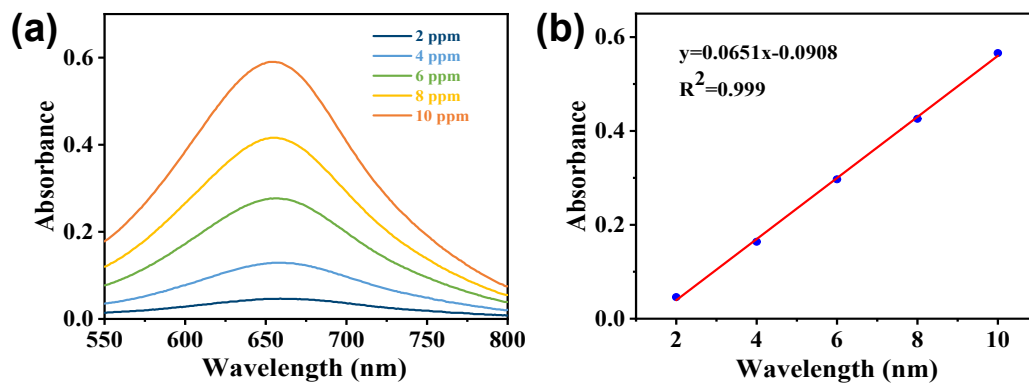
Figure S18 (a) UV-Vis adsorption spectra of standard solution containing different NH_4^+ concentration. (b) The linear standard plot for calculating the concentration of NH_4^+ in liquid products.
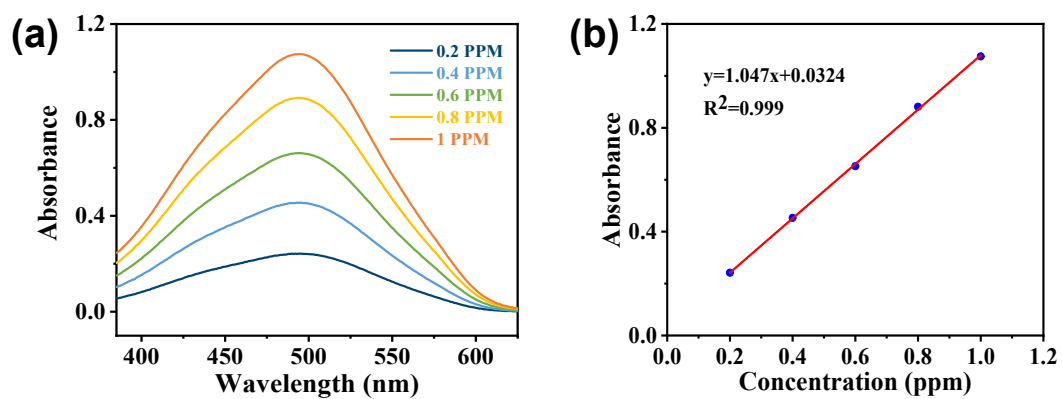
Figure S19 (a) UV-Vis adsorption spectra of standard solution containing different NO_2^- concentration. (b) The linear standard plot for calculating the concentration of NO_2^- in liquid products
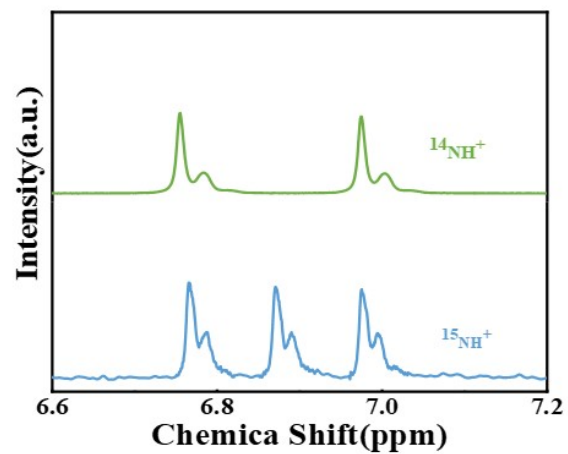
Figure S20 ^{1}H NMR spectra of liquid products produced from the NO_3^-RR using ^{14}N nitrate and ^{15}N nitrate as reactants.
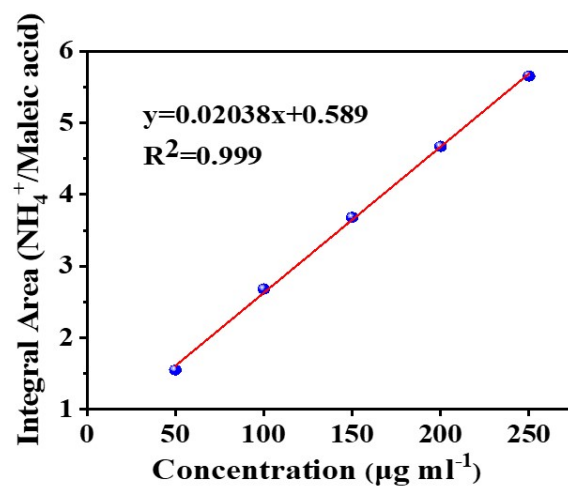
Figure S21 The standard curve of integral area ($^{14}NH^{4+}/C_4H_4O_4$) as a function of $^{14}NH^{4+}$ concentration.
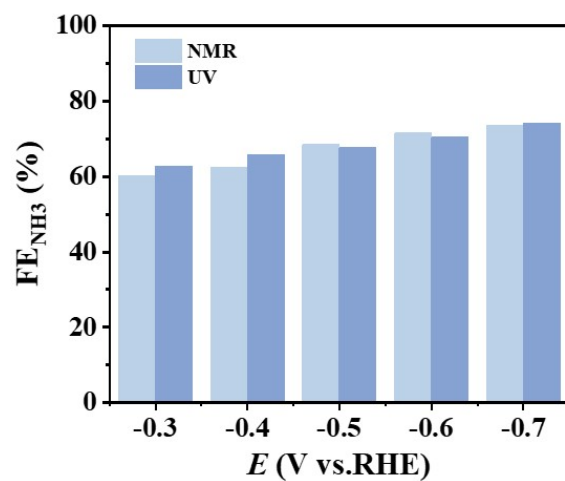
Figure S22 Comparing FE_{NH3} quantified by ^{1}H-NMR and UV-Vis on the Cu-N$_4$.
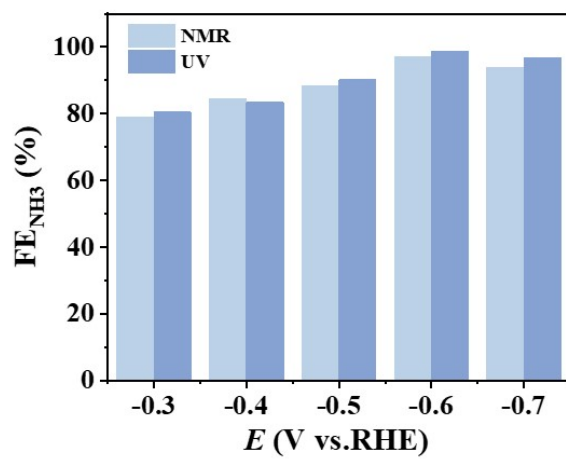
Figure S23 Comparing FE_{NH3} quantified by ^{1}H-NMR and UV-Vis on the Cu-N_4B_2.
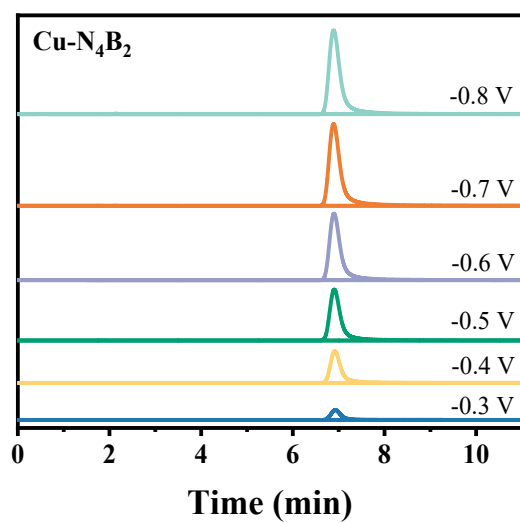
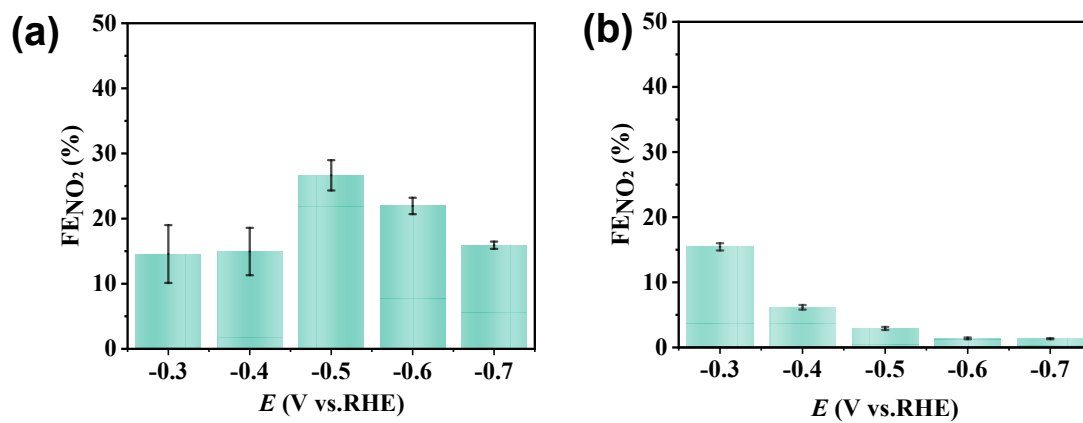**Figure S24** Representative GC of gas products obtained on Cu-N$_4$B$_2$ at the different potential (vs. RHE).

Figure S25 FE_{NO2} of the catalysts (a)Cu-N_4B_2 (b)Cu-N_4.

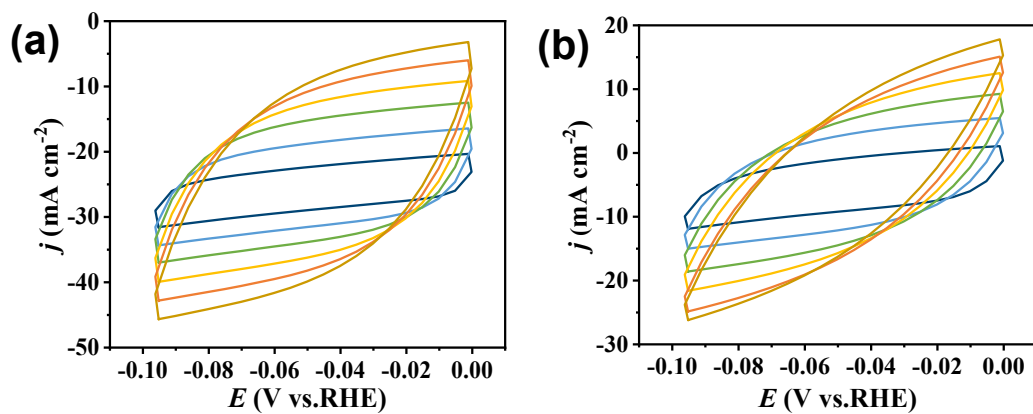**Figure S26** The CV curves at different scan rates for (a)Cu-N$_4$B$_2$ and (b)Cu-N$_4$.
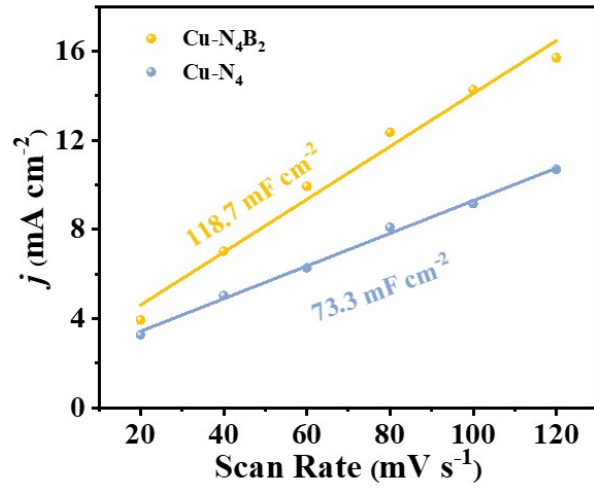
Figure S27 Curves of capacitance Δj ($|j_{charge}\text{-}j_{discharge}|$) as a function of different scan rates for Cu-N$_4$ and Cu-N$_4$B$_2$.
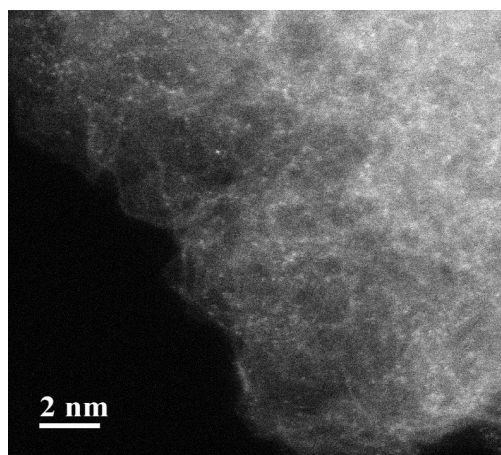
Figure S28 HAADF-STEM images of Cu-N$_4$B$_2$ after continuous NO$_3^-$RR for 30-h.
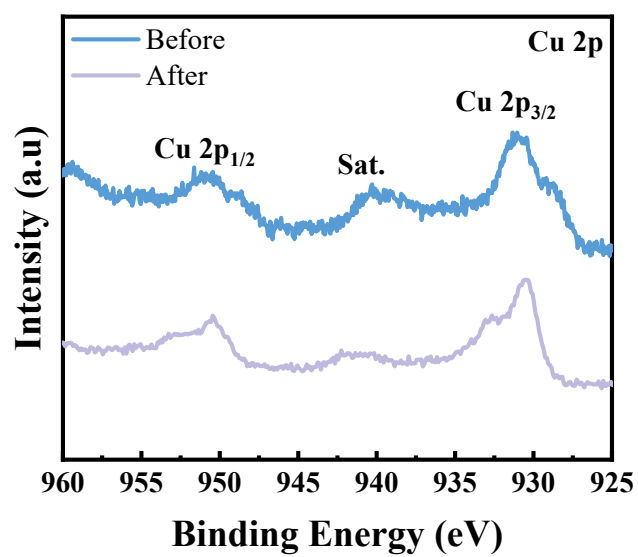
Figure S29 XPS spectra of Cu 2p for Cu-N_4B_2 before and after continuous NO_3^-RR for 30-h.
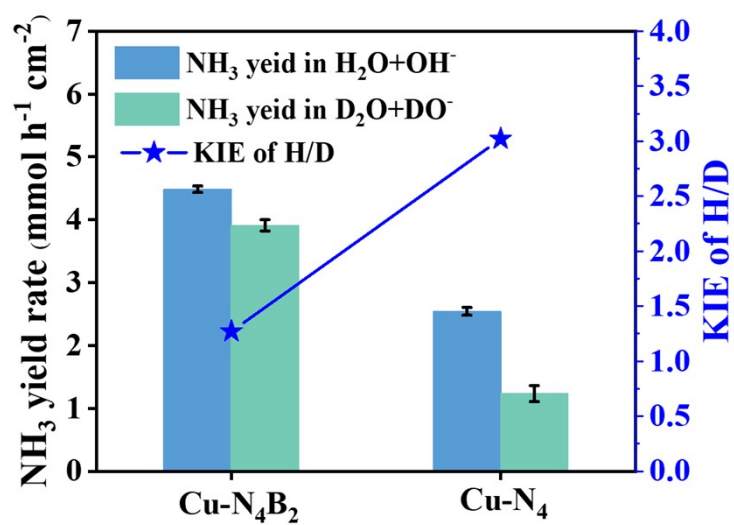
Figure S30 KIE of Cu-N$_4$B$_2$ and Cu-N$_4$Cmeasured at -0.6 V vs. RHE.
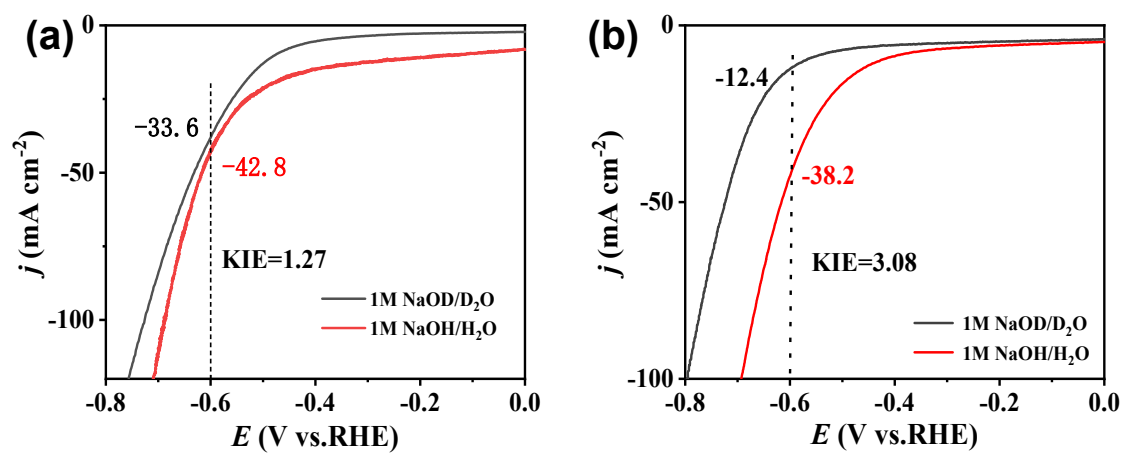
Figure S31 The current density of KIE test on a) Cu-N$_4$B$_2$ and b) Cu-N$_4$.
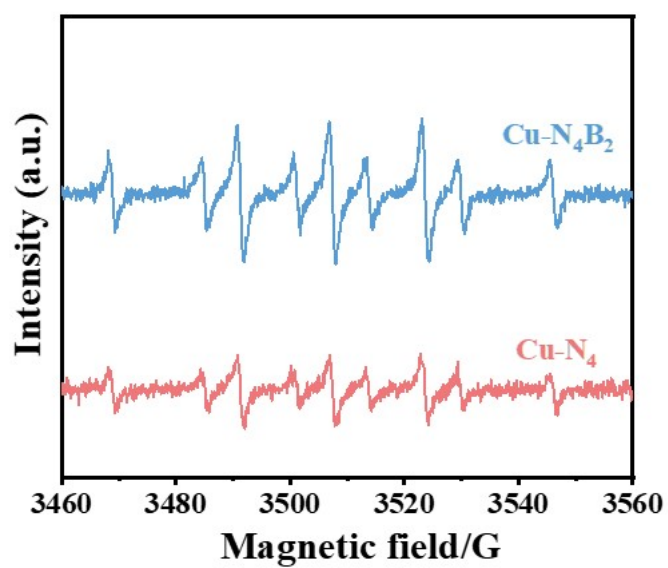
Figure S32 ESR spectra of the solutions obtained after 10 min of NO_3^-RR electrocatalyzed by Cu-N_4B_2 and Cu-N_4. in 1 M KOH under argon using DMPO as the ·H-trapping reagent.
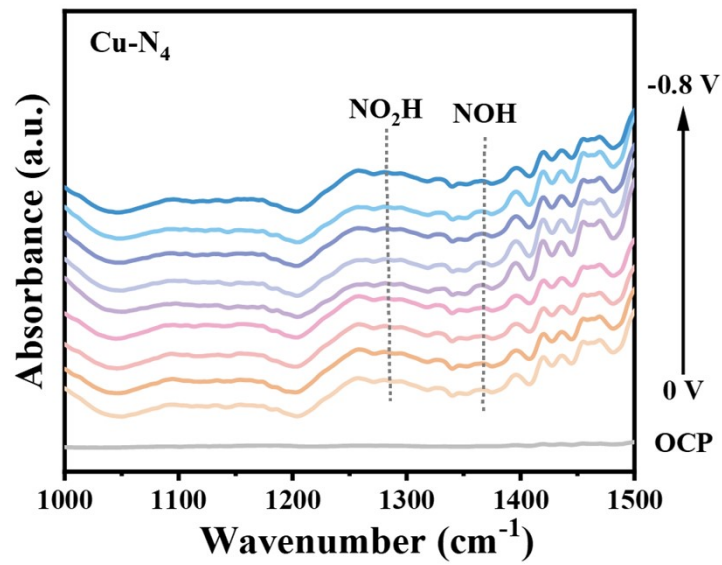
Figure S33 In situ ATR-SEIRAS spectra recorded over Cu-N$_4$ at different applied potentials (vs. RHE).
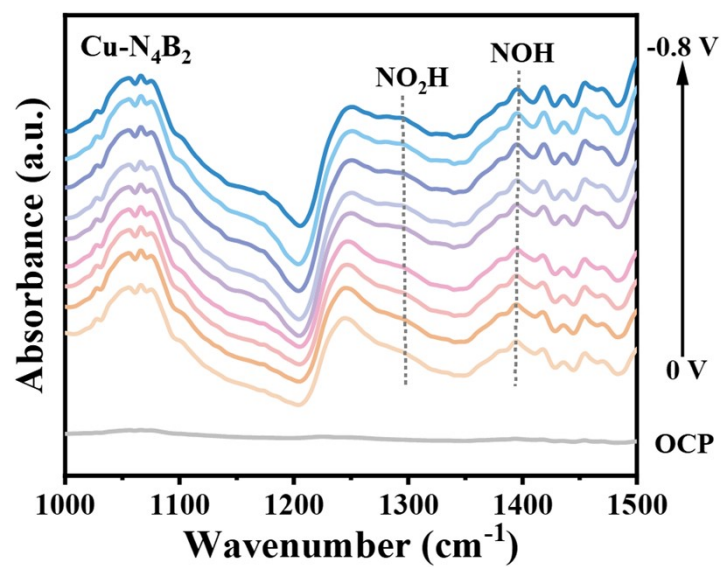
Figure S34 In situ ATR-SEIRAS spectra recorded over Cu-N_4B_2 at different applied potentials (vs. RHE).
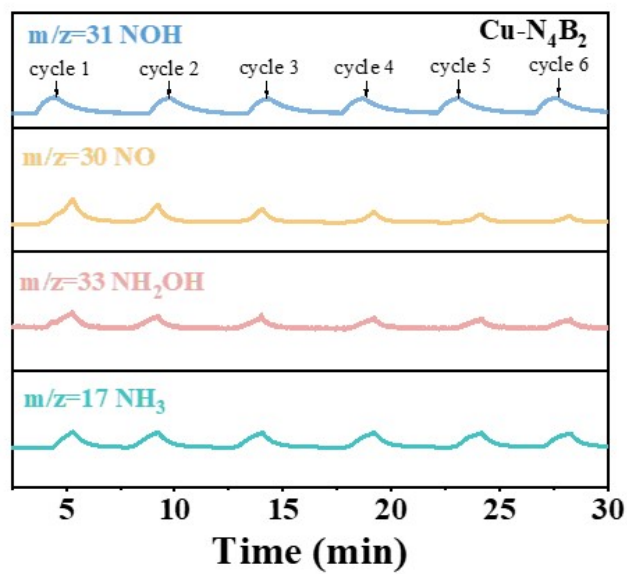
Figure S35 Differential electrochemical mass spectrometry (DEMS) measurements of NO_3^-RR over $Cu-N_4B_2$.
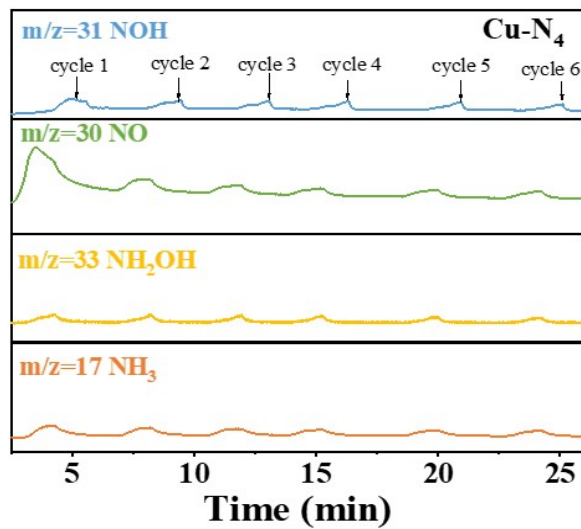
Figure S36 Differential electrochemical mass spectrometry (DEMS) measurements of NO_3^-RR over Cu-N$_4$.
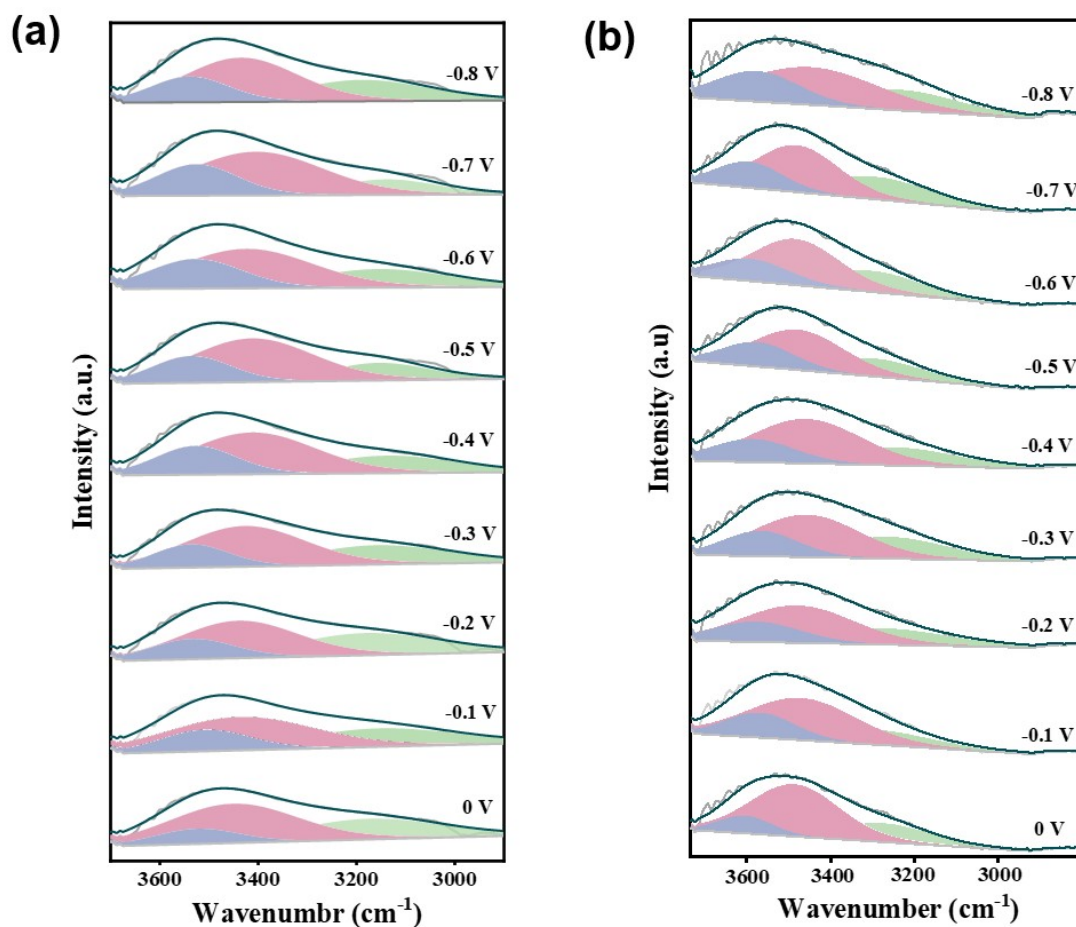
Figure S37 In situ ATR-SEIRAS measurements. Gaussian fits of three O−H stretching modes over (a) Cu-N$_4$B$_2$ and (b) Cu-N$_4$. Potential-dependent relative proportions of interfacial water over. The relative proportion was obtained by dividing the proportion of each component by its corresponding peak area at 0 V to eliminate the experimental errors.
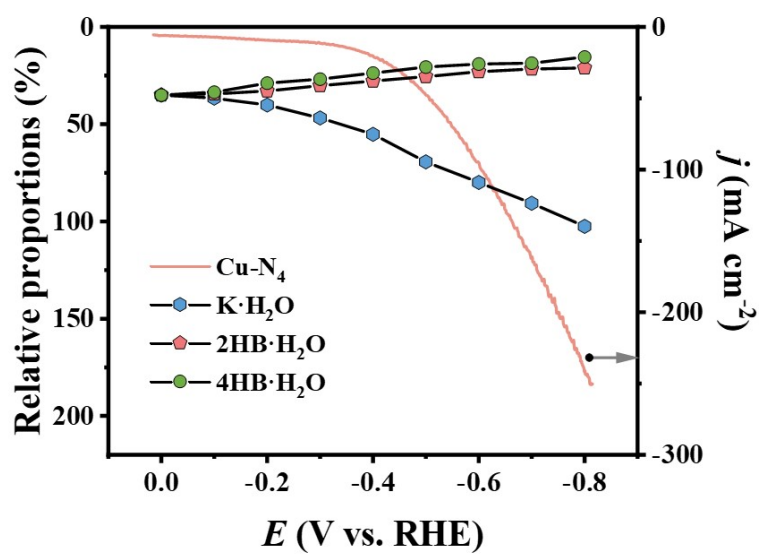
Figure S38 Relative proportions of different types of interfacial H_2O adsorbed on Cu-N_4 with the vary of cathode potentials. The relative proportion was obtained by dividing the proportion of each component by its corresponding peak area at 0 V to eliminate the experimental errors.
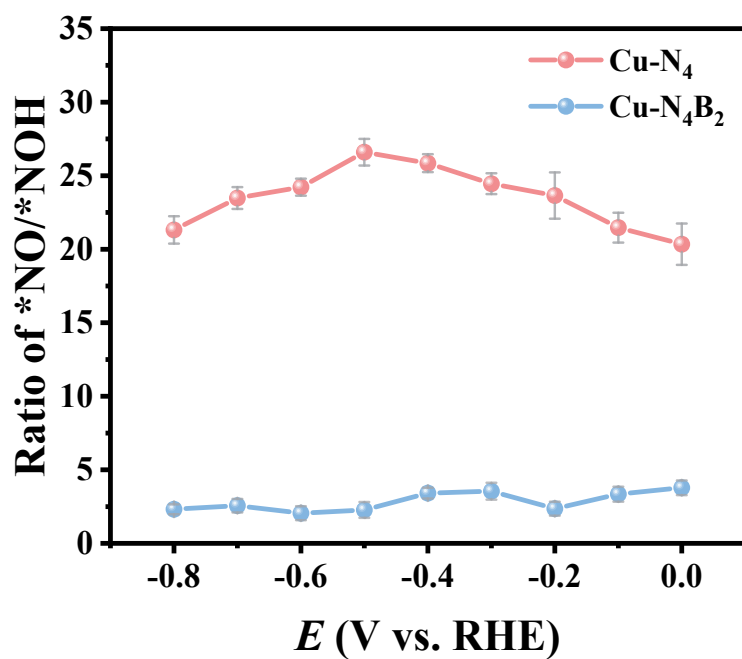
Figure S39 Calculated ratio of $^*NO/^*NOH$ over Cu-N$_4$B$_2$ and Cu-N$_4$. Error bars in figure represent s.d. for each data point (n = 3 independent experiments), and points are average values.
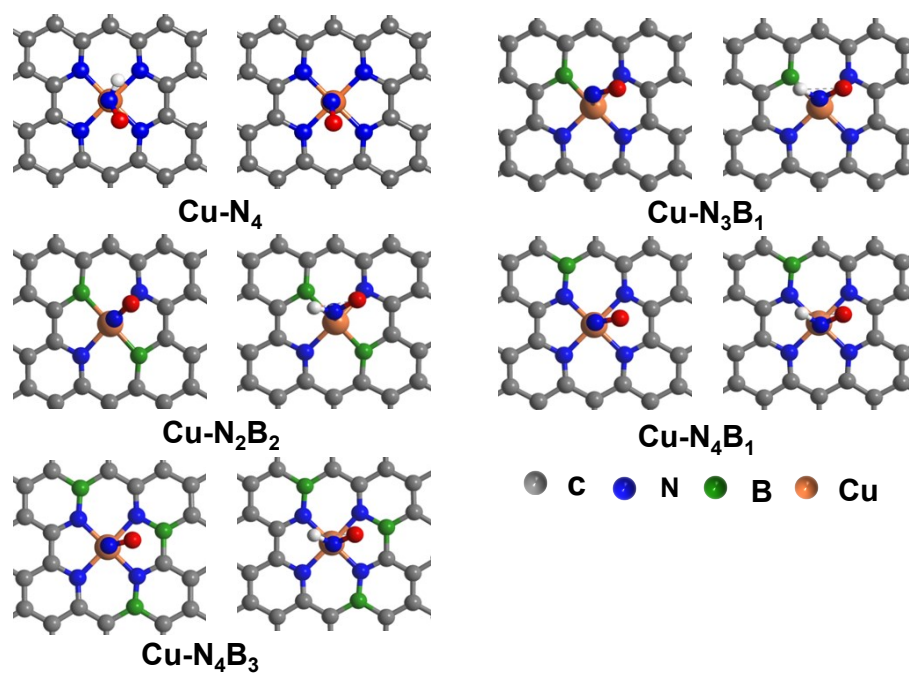
Figure S40 Top view of the optimized atomic structures of Cu-N$_4$, Cu-N$_3$B$_1$, Cu-N$_2$B$_2$, Cu-N$_4$B$_1$ and Cu-N$_4$B$_3$ with absorbed *NO and *NOH intermediates.

Cu-N₂B₂ **Cu-N₃B₁**

Cu-N₄B₁ **Cu-N₄**

Cu-N₄B₂ **Cu-N₄B₃**

● C ● N ● B ● Cu
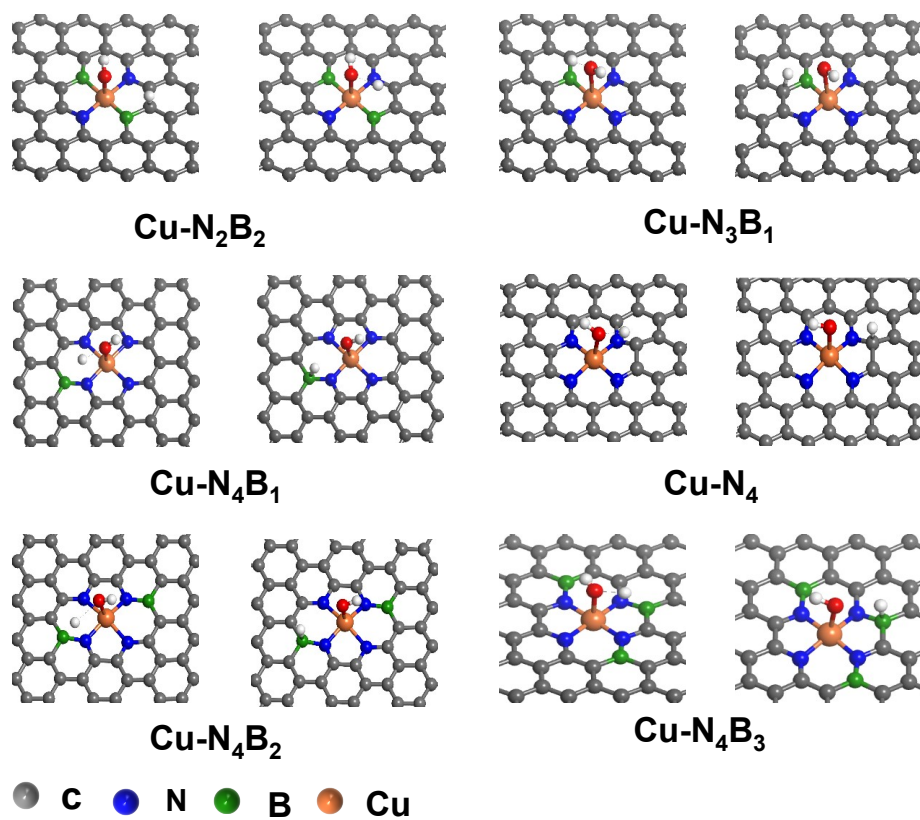
Figure S41 Top view of the optimized atomic structures of Cu-N_4, Cu-N_3B_1, Cu-N_2B_2, Cu-N_4B_1 and Cu-N_4B_3 with absorbed *H_2O intermediates.
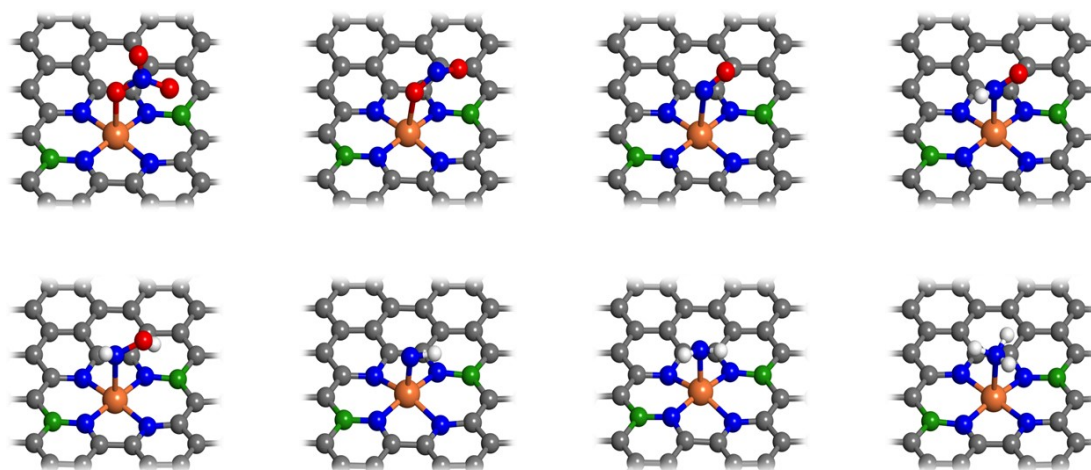
Figure S42 Top view of the optimized atomic structures of Cu-N$_4$, Cu-N$_3$B$_1$, Cu-N$_2$B$_2$, Cu-N$_4$B$_1$ and Cu-N$_4$B$_3$ with absorbed NO$_3^-$RR intermediates.

Table S1. Cu-N bond lengths and corresponding strain in the B/Cu-N-C material.

Sample	Cu-N_1/Å	Cu-N_2/Å	Cu-N_3/Å	Cu-N_4/Å	S1/%	S_2/%	S3/%	S4/%
Cu-N_4	1.92	1.92	1.92	1.92	0.00	0.00	0.00	0.00
Cu-N_3B_1	1.92	1.92	1.92	1.93-Cu-B	0.00	0.00	0.00	0.52
Cu-N_2B_2	1.93	1.93	1.94-Cu-B	1.94-Cu-B	0.52	0.52	1.04	1.04
Cu-N_4B_1	1.87	1.94	1.93	1.91	-2.60	1.04	0.52	-0.52
Cu-N_4B_2	1.86	1.86	1.93	1.93	-3.12	-3.12	0.52	0.52
Cu-N_4B_3	1.85	1.88	1.91	1.94	-3.65	-2.08	-0.52	1.04

Table S2. The component and content of Cu-N_4C and Cu-N_4B_2.

Sample	Cu (wt.%)	N (wt.%)	B (wt.%)	C (wt.%)	O(wt.%)
Cu-N_4	3.33	8.23	/	80.16	8.28
Cu-N_4B_2	3.86	10.23	3.73	72.05	10.13

The element content was determined by the elemental analyzer.

Table S3. Structural parameters extracted from the Cu K-edge EXAFS fitting.

Sample	Path	CN	R (Å)	σ^2	ΔE_0 (eV)	R-factor
Cu-N_4	Cu-N	3.78±0.40	1.94±0.01	0.003	2.56	0.006
Cu-N_4B_2	Cu-N	4.18±0.18	1.92±0.01	0.005	-5.5	0.007
	Cu-B	1.97±0.39	2.64±0.02	0.005	7.6	

[a]*N:* coordination number; [b]*R:* bond distance; [c]σ^2: Debye-Waller factor; [d] ΔE_0: inner potential correction; *R* factor: goodness of fit.

Table S4 Comparing the performance of our synthesized Cu-N$_4$B$_2$ with other reported electrocatalysts for NO$_3^-$RR.

Electrocatalyst	Electrolyte	FE$_{NH3}$	NH$_3$ yield rate (mmol h^{-1} cm^{-2})	Ref.
Cu-N$_4$B$_2$	**1 M KOH + 0.1 M KNO$_3$**	**98.2% (−0.6 V vs. RHE)**	**4.5 (−0.7 V vs. RHE)**	This work
Fe single atom	0.5 M KNO$_3$ + 0.1 M K$_2$SO$_4$	75.0% (−0.66 V vs. RHE)	0.46 (−0.66 V vs. RHE)	[8]
CoS$_2$@TiO$_2$	0.1 M NaOH+ 0.5 M NO$_3^-$	92.80% (−0.7 V vs. RHE)	0.538 (−0.7 V vs. RHE)	[9]
Cu$_2$O	0.5M Na$_2$SO$_4$ + 200ppm KNO$_3$	85.26% (−1.2 V vs. RHE)	0.0786 (−1.2 V vs. RHE)	[10]
Ag/Cu$_2$O	0.5M Na$_2$SO$_4$+100 ppm NO$_3^-$	96.45% (-0.8 V vs. RHE)	3.808 (-0.8 V vs. RHE)	[11]
Cu/Cu$_2$O NWAs	0.5M Na$_2$SO$_4$+200 ppm NO$_3^-$	95.8% (-0.85 V vs. RHE)	0.2449 (-0.85 V vs. RHE)	[12]
FeB$_2$	1 M KOH + 0.1 M KNO$_3$	96.8% (-0.6 V vs. RHE)	1.5 (-0.6 V vs. RHE)	[13]
Co$_1$-P/NPG	0.5 M K$_2$SO$_4$ + 0.1 M KNO$_3$	93.8% (-0.7 V vs. RHE)	0.0572 (-0.7 V vs. RHE)	[14]
Cu-N-C SAC	0.1 M KOH + 0.1 M KNO$_3$	84.7% (-1.0 V vs. RHE)	0.264 (-1.0 V vs. RHE)	[15]
Co-CNP	0.02 M Na$_2$SO$_4$ + 100 mg N-NO$_3^-$	92.0% (-0.69 V vs. RHE)	0.0255 (-0.89 V vs. RHE)	[16]
Co$_3$CuN	0.5 M KOH + 2000 ppm NO$_3^-$	97% (-0.3 V vs. RHE)	0.0268 (-0.3 V vs. RHE)	[17]
NiPr-TPA-COF	0.5 M K$_2$SO$_4$ + 0.3 M KNO$_3$	90% (-1.38 V vs. RHE)	0.147 (-1.38 V vs. RHE)	[18]
Fe$_1$/NC-900	0.1 M K$_2$SO$_4$ + 0.5	86% (-0.7 V vs. RHE)	1.1 (-0.9 V vs. RHE)	[19]

References

1. G. Kresse and J. J. C. m. s. Furthmüller, *Comput.Mater.Sci.*, 1996, **6**, 15-50.

2. J. P. Perdew, K. Burke and M. E Ernzerhof, *Phys. Rev. Lett.*, 1996, **77**, 3865.

3. P. Blöchl, *Matter Mater. Phys.*, 1994, **50**, 17953.

4. G. Kresse and D. Joubert, *Matter Mater. Phys.*, 1999, **59**, 1758.

5. S. Grimme, *Chem.*, 2006, **27**, 1787-1799.

6. S. Grimme, J. Antony, S. Ehrlich and H. Krieg, *J. Chem. Phys.*, 2010, **132**.

7. G. Henkelman and H. Jónsson, *Chem. Phys.*, 2000, **113**, 9978-9985.

8. Z.-Y. Wu, M. Karamad, X. Yong, Q. Huang, D. A. Cullen, P. Zhu, C. Xia, Q. Xiao, M. Shakouri, F.-Y. Chen, J. Y. Kim, Y. Xia, K. Heck, Y. Hu, M. S. Wong, Q. Li, S. Siahrostami and H. Wang, *Nat. Commun.*, 2021, **12**, 2870.

9. X.-E. Zhao, Z. Li, S. Gao, X. Sun and S. Zhu, *Chem. Commun.*, 2022, **58**, 12995-12998.

10. Z. Gong, W. Zhong, Z. He, Q. Liu, H. Chen, D. Zhou, N. Zhang, X. Kang and Y. Chen, *Appl. Catal B Environ.*, 2022, **305**, 121021.

11. H. Yin, X. Zhao, S. Xiong, Y. Peng, Z. Chen, R. Wang, M. Wen, J. Luo, H. Yamashita and J. Li, *J. Catal.*, 2022, **406**, 39-47.

12. Y. Wang, W. Zhou, R. Jia, Y. Yu and B. Zhang, *Angew. Chem. Int. Ed.*, 2020, **59**, 5350-5354.

13. G. Zhang, X. Li, K. Chen, Y. Guo, D. Ma and K. Chu, *Angew. Chem. Int. Ed.*, 2023, **62**, e202300054.

14. J. Ni, J. Yan, F. Li, H. Qi, Q. Xu, C. Su, L. Sun, H. Sun, J. Ding and B. Liu, *Adv. Energy. Mater.*, 2024, 2400065.

15. J. Yang, H. Qi, A. Li, X. Liu, X. Yang, S. Zhang, Q. Zhao, Q. Jiang, Y. Su, L. Zhang, L. Jianfeng, Z. Tian, W. Liu, A. Wang and T. Zhang, *J. Am. Chem. Soc.*, 2022, **144**, 12062-12071.

16. J. Li, M. Li, N. An, S. Zhang, Q. Song, Y. Yang, J. Li and X. Liu, *Proc. Natl. Acad. Sci.*, 2022, **119**, e2123450119.

17. Z. Gong, X. Xiang, W. Zhong, C. Jia, P. Chen, N. Zhang, S. Zhao, W. Liu, Y. Chen and Z. Lin, *Angew. Chem. Int. Ed.*, 2023, **135**, e202308775.

18. F. Lv, M. Sun, Y. Hu, J. Xu, W. Huang, N. Han, B. Huang and Y. Li, *Energy Environ. Sci.*,

2023, **16**, 201-209.

19. L. Liu, T. Xiao, H. Fu, Z. Chen, X. Qu and S. Zheng, *Appl. Catal B Environ.*, 2023, **323**, 122181.